



Effect of crystallographic orientation on residual stress induced in micro-grinding

Man Zhao^{1,2} · Jian Mao¹ · Xia Ji³ · Yixuan Feng² · Steven Y. Liang^{2,3}

Received: 5 June 2020 / Accepted: 29 October 2020 / Published online: 2 January 2021
© Springer-Verlag London Ltd., part of Springer Nature 2021

Abstract

In micro-grinding, the effect of material microstructure on residual stress is significant since the depth of cut is usually smaller than the average grain size. In this paper, the effect of crystallographic orientation (CO) on the distribution of residual stress induced by micro-grinding is investigated. The COs and their volume fractions of workpiece material are quantified by Taylor factor, based on which the models of flow stress and plastic modulus of polycrystalline materials are proposed. Then, the residual stress is calculated based on the micro-grinding force and temperature derived from the flow stress, after the mechanical and thermal loading followed by relaxation process, which are analyzed with the developed plastic modulus. Thereby, the compressive analytical model of micro-grinding-induced residual stress is proposed considering the grinding parameters, wheel topography, and material microstructure. In addition, micro-grinding experiments and residual stress measurements are conducted to verify the models. The prediction of residual stress agrees well with the experimental result. Residual stresses are measured by X-ray techniques, and the results illustrate that the COs of material would influence the state of stress. Finally, the sensitivity analysis is carried out, with the result showing that the effect of CO on residual stress is significant.

Keywords Flow stress · Residual stress · Crystallographic orientation · Taylor factor · Force · Temperature

Nomenclature

A, B, C, m, n	Johnson-Cook parameters
E	Workpiece elasticity modulus
K_w, K_t	Workpiece and wheel elasticity
C_p	Specific heat
b_1	Burger vector
α_1	Material constant
ν	Poisson's ratio
V	Wheel speed
V_w	Workpiece speed or feed rate
l_{oc}	Contact length of the rubbing plane
α_{cr}	The critical rake angle
φ_k	Local shear angle

α_k	Local rake angle
β_k	Local friction angle
τ_s	Shear strength in tangential direction
t	Undeformed chip thickness
D	Grit diameter
C_s	Static cutting edge density
C_d	Dynamic cutting edge density
Φ	Angle between slip plane and cutting plane in grain
φ_1, φ_2	Correction angles
$\sigma_{ij}^{mech}, \sigma_{ij}^{therm}$	Mechanical and thermal stresses
h	Plastic modulus
S_{ij}	Deviatoric stresses
K	Uniaxial normalized radius of the yield surface
$\dot{\epsilon}_{xx}, \dot{\epsilon}_{yy}$	Plastic strain rate
F_{tg}	Tangential force of single grit
F_{ng}	Normal force of single grit
ρ_1	Density of dislocation
ρ	Material density
K	Thermal conductivity
n_{pass}	The number of loading pass
a_p	The depth of cut

✉ Jian Mao
jmiao@sues.edu.cn

¹ School of Mechanical and Automotive Engineering, Shanghai University of Engineering Science, Shanghai, China

² Woodruff School of Mechanical Engineering, Georgia Institute of Technology, Atlanta, GA, USA

³ School of Mechanical Engineering, Donghua University, Shanghai, China

l_c	The total contact length of the primary heat source
T_0, T_m, T_w	Workpiece, ambient, and melting temperature
w	Cutting width
r	The cutting edge radius
M_1	Taylor factor of polycrystalline material
A_s, k_s	Parameters of wheel topography
ε_0	Material constant
ε	Plastic strain
$\dot{\varepsilon}$	Plastic strain rate
ψ	The cone angle of grit
α	Thermal diffusivity
σ	Total flow stress
Ω	Angle between slip direction and cutting direction in grain
ΔT_{wk}	Workpiece temperature rise
ψ	Blending function
G	Elastic shear modulus
α_{ij}	Back stresses
ε_{eff}^p	Effective plastic strain rate

1 Introduction

With the rapid development of miniaturization, micro-grinding technology has been widely used in the cutting edge industries [1]. Micro-grinding-induced residual stress is a crucial parameter and a key index for the surface integrity evaluation [2]. Prediction of the residual stress is inevitable to control and improve the surface quality of the machined components. However, the mechanism of micro-grinding-induced residual stress and the influence factors are still not yet fully understood. Therefore, it is a challenge for the engineers to accurately predict the residual stress induced in micro-grinding nowadays.

Numerous researchers have focused on investigating the mechanism and the influence factors of residual stress induced in the grinding process [3–7]. Thermal expansion and contraction, phase transition (for multi-phases material), and plastic deformation are the major causes for residual stress induced in grinding [8]. Fergani et al. [9] suggested that temperature rise is the main cause of tensile residual stress, which induces the thermal expansion and contraction in grinding process, and developed a physics-based model of critical temperature for activating the tensile residual stress. Afterwards, Shao et al. [10] developed a model of residual stress distribution accounting for mechanical and thermal loading using mathematical method, calculated the mechanical and thermal stress history in grinding process by assuming two-dimensional Hertz contact, and predicted the relaxation process of unloading based on the hybrid algorithm. Finally, the predictive model of grinding residual stress was validated by the experimental data. Shi et al. [11] investigated the

surface residual stress of dry grinding by the finite element method (FEM) and revealed the mechanism that phase transformation mainly causes compressive stress. Shen et al. [12] experimentally investigated the variations of residual stress induced in grinding of maraging steel. The results show that the mechanical effect is dominant in dry grinding. In addition, Guo et al. [13] reviewed the research of residual stress measurement methods over the past 5 years. Zhu et al. [14] reported that the robotic grinding process could solve the problem of precision machining of small-scale complex surfaces and control the tensile residual stress by decreasing the tangential force precisely

Grinding conditions, the topography and property of grinding wheel, and cooling conditions are the three major influence factors of grinding residual stress [3]. The topography of grinding wheel was modeled using a different method, and the effects on grinding temperature and force were analyzed in Ref. [15–17]. The effects of grinding parameters on the residual stress distribution were experimentally analyzed in Ref. [18], and results show that peak compressive residual stress increases greatly with the growing wheel speed, and the penetration depth is positively related to wheel speed and grinding depth. Wu et al. [19] suggested that the high-speed grinding process could help substantially improve the workpiece integrity by the controlled residual stresses in a higher material removal rate. Jiang et al. [20] introduced a residual stress volume model to evaluate the effects of sequential cuts for the generated surface and subsurface residual stresses. The mentioned investigations analyzed the mechanism of residual stress and the complicated influence factors in the grinding process. Although a micro-grinding process is similar with a conventional grinding process, micro-grinding is distinctive due to size and the crystal effect. In addition to the mentioned mechanism and influence factors, the effect of material microstructure on the mechanism of micro-grinding-induced residual stress in the process needs to be considered.

Material microstructure covers grain size, dislocation density, phases, and crystal orientation. Ding et al. [21] investigated the phase transition mechanism in micro-grinding-induced residual stress generation and predicated the residual stress by considering the effect of phase transformation using FEM. The result shows that tensile stress decreases with the transformation from ferrite to austenite, and the maximum tensile stress is smaller when considering phase transition. The phase transition model was built by fitting measured data. In milling and turning process, the residual stress was predicted considering grain size effect which was quantitatively expressed by Hall-Petch model [22–25]. The proposed predictive model matches the trends of experimental measurements well. Similarly, the Hall-Petch model could be utilized to analyze the effect of grain size on micro-grinding-induced residual stress. Li et al. [26] proposed a crystal plasticity model based on the texture representative volume element to predict Bauschinger effect, which took the effect of COs into account. However, this model incorporated into the FEM method was

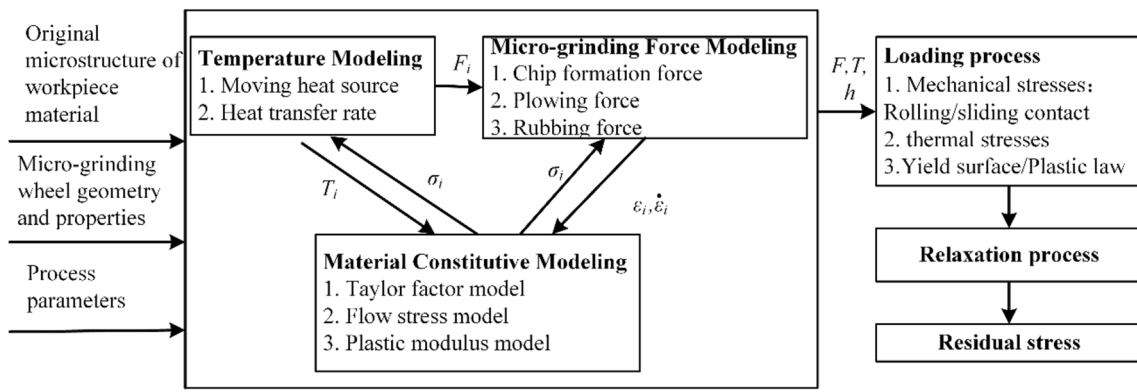


Fig. 1 Residual stress flowchart

only used to simulate the relationship between strain and stress during cyclic loading, but not residual stress induced in machining. Wang et al. [27] revealed that the residual stress relaxation had different influences on the dislocation density and the strain energy within grain with different types of orientation. However, the investigation just analyzed the effect qualitatively. In Ref [28], the deformation mechanism is suggested to be related to the formation of dislocations and stacking faults and the distortion of atomic planes, and grinding force model of the grinding of YAG single crystals is developed based on the deformation mechanism of a crystal solid. Zhao et al. [15, 16] proposed a Taylor factor model to estimate the effects of COs on micro-grinding process. In addition, the force and temperature models were developed considering Taylor factor, and the results show that the effects of COs on micro-grinding force and temperature are prominent. To the best of our knowledge, the COs of polycrystalline material and its effect on the micro-grinding-induced residual have never been investigated comprehensively.

In this paper, the plastic modulus and flow stress models are developed with consideration of the Taylor factor, based on which, the mechanical and thermal loading and relaxation

process are predicted. Therefore, the micro-grinding-induced residual stress profile is obtained considering the material microstructure. Finally, the proposed model is validated by the experimental data.

2 Analytical model

To understand the micro-grinding-induced residual stress clearly, the paper analytically investigates this process by focusing on the flow stress and plastic modulus modeling, mechanical and thermal loading, and relaxation. The residual stress flowchart is shown in Fig. 1.

As shown in Fig. 1, the original microstructure of workpiece material, wheel geometry and properties, and process parameters are the input parameters for the material constitutive model, the micro-grinding force model, and the temperature model. In addition, the micro-grinding force and temperature are coupled by flow stress model. Finally, the force, temperature, and plastic modulus decide the mechanical and thermal stress distribution and the residual stress after relaxation.

2.1 Microstructure analysis of workpiece

Alloy aluminum 7075-T6 is a single-phase metal with face-centered cubic structure. In the chip formation process of micro-grinding, the material dislocation slip is

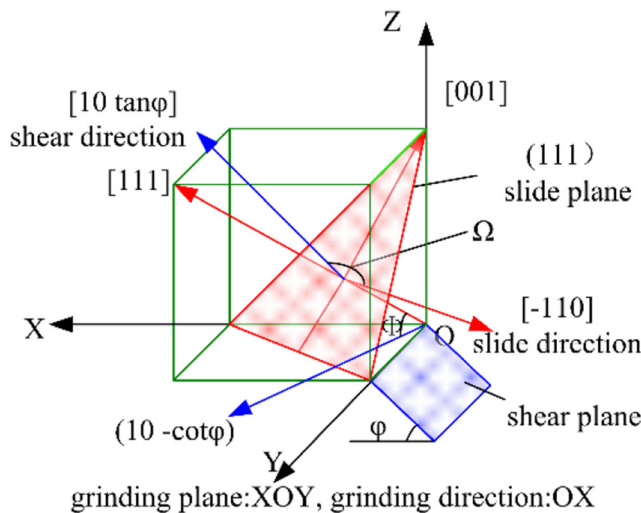


Fig. 2 Dislocation slip map in one slip system

Table 1 The process parameters of milling for the corresponding Taylor factor

Process parameters	Sample no.			
	1	2	3	4
Rotate speed (r/min)	8000			
Feed rate (mm/tooth)	0.2			
Depth of cut (mm)	1	1	2	2
Taylor factor	5.60	8.44	9.11	9.75

the main plastic deformation. The dislocation slip map in one slip system is shown in Fig. 2. where Φ denotes the angle between shear plane and slide plane in grain; Ω stands for the angle between slide direction and shear direction in grain; φ is the shear angle, the normal vector of the shear plane is $[1 \ 0 \ -\cot\varphi]$, and the shear direction is $[1 \ 0 \ \tan\varphi]$. The acting force on the shear plane in the shear direction causes the crystal gliding of the material which results in plastic deformation. However, crystal gliding may not happen in the shear plane but the slide plane, due to the lower energy expended. As a result, the shear force and the deformation are decided by the angles between shear plane and sliding plane. If the angle is 0° , the shear force is the minimum.

Each crystal system has at least five activated different slip systems, in which the slide plane orientation and slide direction are different. When crystal rotates, the normal vector of slide plane and the vector of slide direction are calculated according to the law: the normal vector \mathbf{n}^r of rotated slide plane is $\mathbf{n}^r = \mathbf{B} \times \mathbf{n}$; the vector of rotated slide direction \mathbf{m}^r is $\mathbf{m}^r = \mathbf{B} \times \mathbf{m}$, and $\mathbf{B} = \mathbf{Z}_2 \mathbf{X} \mathbf{Z}_1$.

$$\begin{aligned} Z_1 &= \begin{pmatrix} \cos\phi_1 & \sin\phi_1 & 0 \\ -\sin\phi_1 & \cos\phi_1 & 0 \\ 0 & 0 & 1 \end{pmatrix}, \\ X &= \begin{pmatrix} 1 & 0 & 0 \\ 0 & \cos\phi & \sin\phi \\ 0 & -\sin\phi & \cos\phi \end{pmatrix}, \\ Z_2 &= \begin{pmatrix} \cos\phi_2 & \sin\phi_2 & 0 \\ -\sin\phi_2 & \cos\phi_2 & 0 \\ 0 & 0 & 1 \end{pmatrix} \end{aligned} \tag{1}$$

where ϕ_1, ϕ, ϕ_2 are Euler angles, which account for the COs and are measured by electron backscatter diffraction (EBSD). The Taylor factor model of single grain can be expressed as follows:

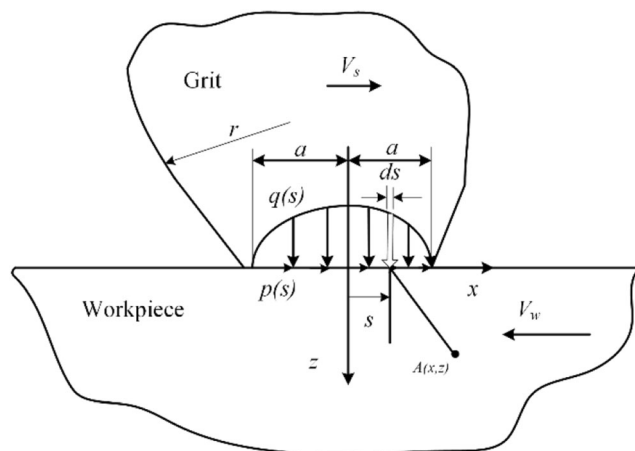


Fig. 3 Stress resulting from mechanical load

$$M^F = \sum_{i=1}^N 1/(\cos\Phi_i \cos\Omega_i) \tag{2}$$

where N refers to the number of total activated slip systems. The Taylor factor model of polycrystalline material is expressed as:

$$M_1 = \sum_{j=1}^{N_1} f_j \times M_j^F \tag{3}$$

where f_j is the orientation distribution function (ODF) of j th CO, and N_1 is the number of COs in the material.

Due to the different micro-textures in the rolling direction (RD) and the normal direction (ND) of the AA7075-T6 plate [29], the microstructures of samples 1 and 3 from RD and samples 2 and 4 from ND are different. As a result, four samples of AA7075-T6 are obtained by milling with different process parameters from a single AA7075-T6 plate. The

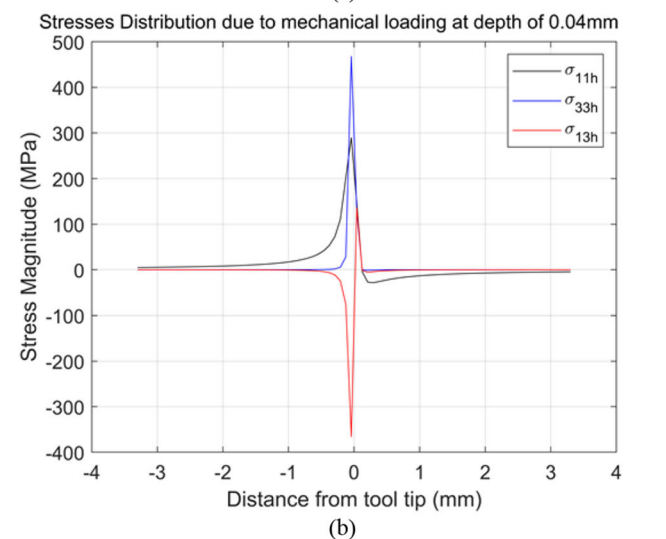
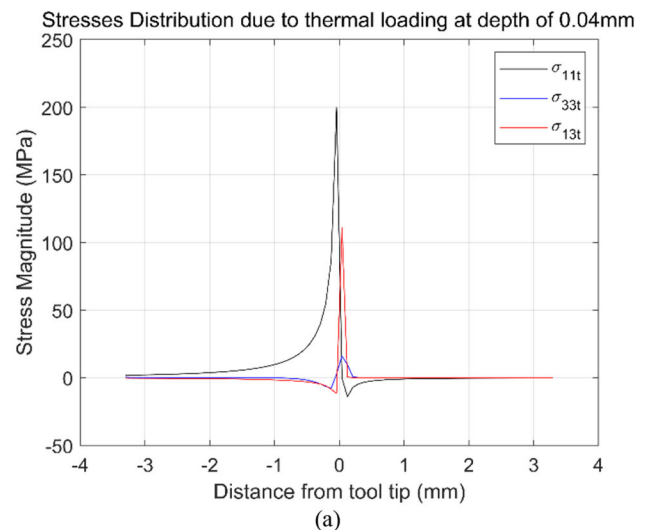


Fig. 4 The predicted stress distributions under a mechanical loading and b thermal loading

process parameters and the corresponding Taylor factor calculated from the proposed model are listed in Table 1.

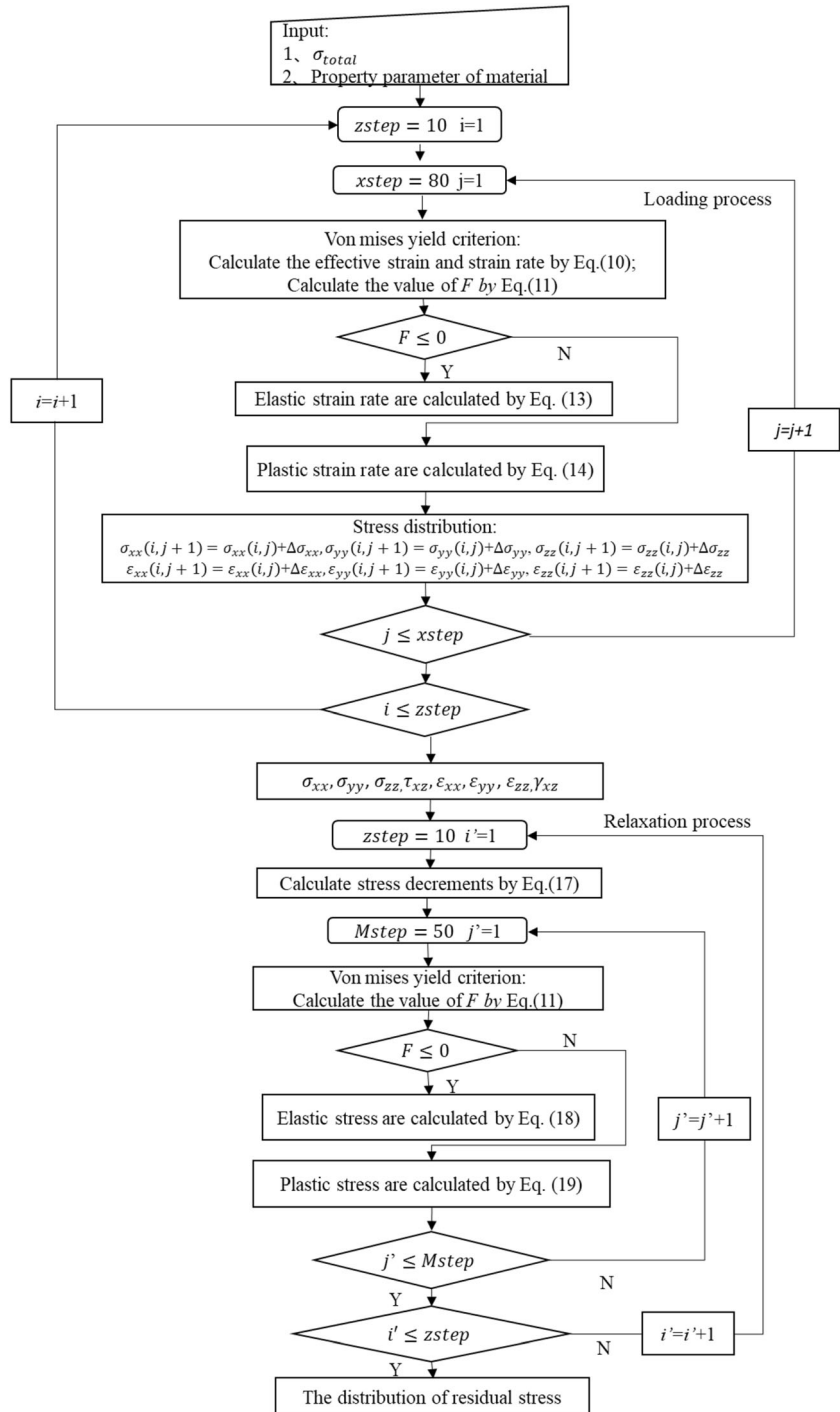
$$\sigma = (A + B\varepsilon^n) \left(1 + C \ln \frac{\dot{\varepsilon}}{\varepsilon_0} \right) \left(1 - \left(\frac{T_0 - T_w}{T_m - T_w} \right)^m \right) + M_1 \alpha_1 G b_1 \sqrt{\rho_1} + K_{HP} / \sqrt{D_d} \tag{4}$$

2.2 Flow stress and plastic modeling

The flow stress model considering thermal and athermal effects is shown as follows:

where $A, B, C, m,$ and n are the Johnson-Cook parameters for materials, ε is the effective strain, $\dot{\varepsilon}$ is the effective strain rate, ε_0 is the reference strain, which is 1 s^{-1} for alloy aluminum

Fig. 5 Calculation procedure chart of residual stress



[17], T_w is room temperature (20 °C), α_1 is the geometrical constant, M_1 refers to the Taylor factor, b_1 is the Burgers vector, ρ_1 denotes the dislocation density, and G is the elasticity modulus. The Hall-Petch index K_{HP} is computed by $K_{HP} = M_1 \sqrt{\frac{\tau_b A G b}{(1-\nu)\pi}}$, $\tau_b = 0.057G$, and ν is the Poisson ratio. All of the properties of materials refer to Ref. [15].

This research made an assumption that the hardening law is linear. So the plastic modulus in the micro-grinding process is the same with that in the hardening test. The constant B in the Johnson-Cook model is equal to the plastic modulus under the linear hardening condition. For the traditional calculation, the constant B is obtained by fitting the experiment data. In the research, h is given as the function of hardness, strain, and microstructure as:

$$h = \left(\frac{H_v}{0.927C} A + M_1 \alpha_1 G b_1 \sqrt{\rho_1} + K_{HP} / \sqrt{D_d} \right) / \varepsilon^n \quad (5)$$

Under the assumption of the linear hardening law, the plastic modulus is a constant for the same material. Therefore, the plastic modulus calculated in the hardening test is the same with that in the micro-grinding process. And the strain in the hardening test is $\varepsilon = 0.08$.

Then, the total grinding force of single grit in tangential and normal directions are calculated by

$$\begin{cases} F_{tg} = F_{tg, shearing} + F_{tg, plowing} + F_{tg, rubbing} \\ F_{ng} = F_{ng, shearing} + F_{ng, plowing} + F_{ng, rubbing} \end{cases} \quad (6)$$

where F_{ng} , F_{tg} , $F_{ng, shear}$, $F_{ng, plow}$, $F_{ng, plow}$, $F_{ng, plow}$, $F_{ng, rubbing}$, and $F_{ng, rubbing}$ are the forces in tangential and the traverse directions.

The forces of the whole wheel are calculated as the multiplication of average single grit force and the number of active cutting edges,

$$\begin{cases} F_t = C_d w l_c F_{tg} \\ F_n = C_d w l_c F_{ng} \end{cases} \quad (7)$$

where the total contact length l_c is expressed as $l_c = (a_p D_c + 8R_r F_{ng} D_c (K_w + K_t))^{1/2}$, where a_p is the depth of cut, D_c is the effective diameter, and K_w and K_t are the workpiece and wheel elasticity, respectively.

The total grinding heat q_t induced by the moving heat source can be expressed as

$$q_t = F_t (V + V_w) / (l_c \times w) \quad (8)$$

The temperature response of the point M in the workpiece can be described by moving heat source model [30]:

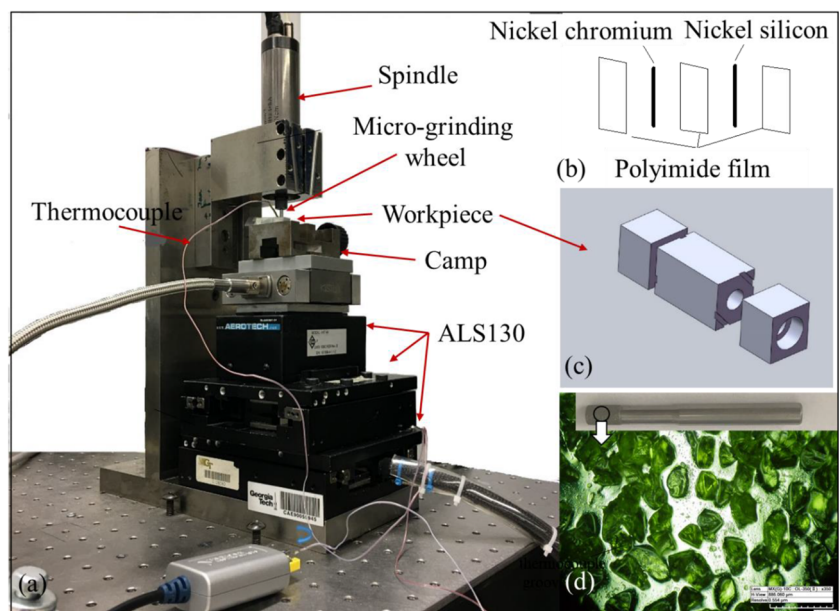
$$T_{(X,Z)} = \frac{q_w}{\pi K_w} \int_{-l_c}^0 f(\zeta_i) \cdot \exp\left(\frac{-V_w(X-l_i)}{2\alpha_w}\right) \cdot K_0 \left\{ \frac{V_w [(X-l_i)^2 + Z^2]^{1/2}}{2\alpha_w} \right\} d\zeta_i \quad (9)$$

where K_0 is the second kind modified Bessel function and α_w is the thermal diffusivity of the workpiece.

2.3 Mechanical and thermal loading histories

The calculation of residual stress induced by mechanical and thermal load considers the stress loading and stress relaxation in micro-grinding. Based on the equivalent micro-grinding conditions, the normal force F_{ng} and the tangential force F_{tg}

Fig. 6 Schematic diagram of micro-grinding: **a** miniaturized CNC grinding tool, **b** single-pole thermocouple of nickel chromium and nickel silicon, **c** workpiece with grooves, and **d** micro-grinding topography



of a single grit as well as the temperature field T are predicted using the previously proposed model [31, 32]. During the loading process, the mechanical stress is induced by the localized interactions between abrasive grains and the workpiece. At the local scale, the distributed loads including tangential pressure $p(s)$ and normal pressure $q(s)$ are generated from the normal force and tangential force of single grit respectively, as shown in Fig. 3.

The stresses at any point $A(x, z)$ are computed as follows:

$$\begin{aligned} \sigma_{xx}^{\text{mech}}(x, z) &= -\frac{2z}{\pi} \int_{-a}^a \frac{p(s)(x-s)^2}{[(x-s)^2 + z^2]^2} ds - \frac{2}{\pi} \int_{-a}^a \frac{q(s)(x-s)^3}{[(x-s)^2 + z^2]^2} ds \quad (10) \\ \sigma_{zz}^{\text{mech}}(x, z) &= -\frac{2z^3}{\pi} \int_{-a}^a \frac{p(s)}{[(x-s)^2 + z^2]^2} ds - \frac{2z^2}{\pi} \int_{-a}^a \frac{q(s)(x-s)}{[(x-s)^2 + z^2]^2} ds \\ \sigma_{xz}^{\text{mech}}(x, z) &= -\frac{2z^2}{\pi} \int_{-a}^a \frac{p(s)(x-s)}{[(x-s)^2 + z^2]^2} ds - \frac{2z}{\pi} \int_{-a}^a \frac{q(s)(x-s)^2}{[(x-s)^2 + z^2]^2} ds \\ \sigma_{yy}^{\text{mech}}(x, z) &= \nu(\sigma_{xx}^{\text{mech}}(x, z) + \sigma_{zz}^{\text{mech}}(x, z)) \end{aligned}$$

$$\begin{aligned} \sigma_{xx}^{\text{therm}}(x, z) &= -\frac{\alpha E}{1-2\nu} \int_0^{+\infty} \int_{-\infty}^{+\infty} \left(G_{xh} \frac{\partial T}{\partial x}(x, z) + G_{xv} \frac{\partial T}{\partial x}(x, z) \right) dx dz + \frac{2z}{\pi} \int_{-\infty}^{+\infty} \frac{p(t)(t-x)^2}{((t-x)^2 + z^2)^2} dt - \frac{\alpha E T(x, z)}{1-2\nu} \\ \sigma_{zz}^{\text{therm}}(x, z) &= -\frac{\alpha E}{1-2\nu} \int_0^{+\infty} \int_{-\infty}^{+\infty} \left(G_{zh} \frac{\partial T}{\partial x}(x, z) + G_{zv} \frac{\partial T}{\partial x}(x, z) \right) dx dz + \frac{2z^3}{\pi} \int_{-\infty}^{+\infty} \frac{p(t)(t-x)^2}{((t-x)^2 + z^2)^2} dt - \frac{\alpha E T(x, z)}{1-2\nu} \quad (12) \\ \sigma_{xz}^{\text{therm}}(x, z) &= -\frac{\alpha E}{1-2\nu} \int_0^{+\infty} \int_{-\infty}^{+\infty} \left(G_{xzh} \frac{\partial T}{\partial x}(x, z) + G_{xzv} \frac{\partial T}{\partial x}(x, z) \right) dx dz + \frac{2z^2}{\pi} \int_{-\infty}^{+\infty} \frac{p(t)(t-x)^2}{((t-x)^2 + z^2)^2} dt \\ \sigma_{yy}^{\text{therm}}(x, z) &= \sigma_{xx}^{\text{therm}}(x, z) + \sigma_{zz}^{\text{therm}}(x, z) \end{aligned}$$

where $p(t) = \frac{\alpha E T(x, z=0)}{1-2\nu}$, α is thermal expansion of material, and $(G_{xh}, G_{zh}, G_{xzh}, G_{xv}, G_{zv}, G_{xzv})$ are plain strain Green's functions [34].

In the micro-grinding process, thermal stress history is obtained considering a single loading pass. However, the mechanical loading is repeated, because the grit travels at a speed of $(V_w + V_s)$ which is much higher than the feed rate V_w . Moreover, the contact length l_c is larger than the average distance between active grits l_0 . The number of loading passes is given by Eq. (13)

$$n_{\text{pass}} = (l_c/l_0)(V_w + V_s)/V_w \quad (13)$$

At the depth of 0.04 mm into the workpiece, the predicted stress distributions produced by mechanical and thermal loading under the grinding condition (6.28 m/s wheel speed, 10 μm depth of cut, and 10 mm/min feed rate) are shown in Fig. 4. The peak stresses appear near the tool tip, since the force and temperature reach the maximum value. Additionally, the adding value of the peak stresses induced by mechanical and thermal loading is higher than the yield

where a is equal to the radius r of the single grit.

The Hertzian pressure p_0 induced by the normal load of single grit and the shear stress τ are calculated using Eq. (7).

$$p_0 = \frac{3F_{\text{ng}}}{2\pi a^2} \tau = \frac{F_{\text{tg}}}{\pi a^2} \quad (11)$$

The thermal stresses induced by temperature T are calculated based on the Timoshenko thermoelasticity theory [33], which are given as [9]:

stress of AA7075-T6. As a result, plastic deformation and hardening are considered in the next section to get the true stress distribution.

2.4 Kinematic hardening and relaxation process

To decide whether the plastic deformation occurs during loading, the von Mises yield criterion is checked in material with the effective strain and strain rate calculated as

$$\begin{aligned} \varepsilon_{\text{eff}}^p &= \frac{\sqrt{2}}{3} \sqrt{(\varepsilon_{xx}^p - \varepsilon_{yy}^p)^2 + (\varepsilon_{yy}^p - \varepsilon_{zz}^p)^2 + (\varepsilon_{zz}^p - \varepsilon_{xx}^p)^2 + 6(\varepsilon_{xz}^p)^2} \\ \dot{\varepsilon}_{\text{eff}}^p &= \sqrt{\frac{2}{3}} \sqrt{\left(\dot{\varepsilon}_{xx}^p\right)^2 + \left(\dot{\varepsilon}_{yy}^p\right)^2 + \left(\dot{\varepsilon}_{zz}^p\right)^2 + 2\left(\dot{\varepsilon}_{xz}^p\right)^2} \quad (14) \end{aligned}$$

The material flow stress could be calculated by Eq. (1) and the yielding criterion based on kinematic hardening is

$$F = \frac{3}{2} (S_{ij} - \alpha_{ij})(S_{ij} - \alpha_{ij}) - \sigma^2 = 0 \quad (15)$$

Table 2 The topography parameters

A_s	K_s	$2r$ (um)	ψ [rad]
$6.44e^{-5}$	02.62	26	2.11

where $S_{ij} = \sigma_{ij} - (\sigma_{kk}/3)\delta_{ij}$ is the deviatoric stress, α_{ij} is the backstress, and σ is flow stress, and the backstress $\dot{\alpha}_{ij} = \langle \dot{S}_{ij} n_{mn} \rangle n_{ij}$.

The elastic strain rate is calculated as

$$\dot{\epsilon}_{xx} = \frac{1}{E} [\dot{\sigma}_{xx} - \nu(\dot{\sigma}_{yy} + \dot{\sigma}_{zz})] + \alpha \Delta T \quad \epsilon_{yy} = \frac{1}{E} [\dot{\sigma}_{yy} - \nu(\dot{\sigma}_{xx} + \dot{\sigma}_{zz})] \quad (16)$$

The effective plastic strain rate is calculated as

$$\dot{\epsilon}_{ij}^p = \frac{1}{h} \langle \dot{S}_{ij} n_{mn} \rangle n_{ij} \quad (17)$$

where $n_{ij} = \sqrt{3/2}(S_{ij} - \alpha_{ij}) / K$.

For the plastic loading, the strain rate is calculated as

$$\begin{aligned} \dot{\epsilon}_{xx} &= \frac{1}{E} [\dot{\sigma}_{xx} - \nu(\dot{\sigma}_{yy} + \dot{\sigma}_{zz}^*)] + \frac{1}{h} (\dot{\sigma}_{xx} n_{xx} + \dot{\sigma}_{yy} n_{yy} + \dot{\sigma}_{zz}^* n_{zz} + 2\dot{\tau}_{xz}^* n_{xz}) n_{xx} \\ &= \psi \left(\frac{1}{E} [\dot{\sigma}_{xx} - \nu(\dot{\sigma}_{yy} + \dot{\sigma}_{zz}^*)] + \frac{1}{h} (\dot{\sigma}_{xx} n_{xx} + \dot{\sigma}_{yy} n_{yy} + \dot{\sigma}_{zz}^* n_{zz} + 2\dot{\tau}_{xz}^* n_{xz}) n_{xx} \right) \end{aligned} \quad (18)$$

Blending function ψ is developed by McDowell with the hybrid algorithm [35]. The blending function is given as

$$\psi = 1 - \exp(-\kappa(3h/2G)) \quad (19)$$

where G is the elastic shear modulus and κ is an algorithm constant. The plastic modulus h is significantly influenced by the microstructure of the material.

After the loading process, the stress and strain should meet to the boundary conditions as following

$$\begin{aligned} (\epsilon_{xx})_r &= 0 \quad (\sigma_{xx})_r = f_1(z) \quad (\epsilon_{yy})_r = 0 \quad (\sigma_{yy})_r = f_2(z) \\ (\epsilon_{zz})_r &= f_3(z) \quad (\sigma_{zz})_r = 0 \quad (\gamma_{xz})_r = f_4(z) \quad (\tau_{xz})_r = 0 \end{aligned} \quad (20)$$

To meet the boundary conditions, the stresses relax after each cycle of loading, and the stress decrements as follows:

Table 3 The micro-grinding parameter combinations

Case number	Wheel speed (m/s)	Feed rate (mm/min)	Depth of cut (μm)	Taylor factor
1	1.57	20	30	9.75
2	6.28	1	20	9.75
3	9.42	10	10	9.75

$$\Delta\sigma_{zz} = -\frac{\sigma_{zz}^R}{M} \Delta\tau_{xz} = -\frac{\tau_{xz}^R}{M} \Delta\epsilon_{xx} = -\frac{\epsilon_{xx}^R}{M} \quad (21)$$

where M is the relaxation steps.

In the stress relaxation process, two material behaviors may occur. For purely elastic relaxation, the increments stress for σ_{xx} and σ_{yy} are calculated as

$$\begin{aligned} \Delta\sigma_{xx} &= \frac{(1 + \nu)(\Delta\sigma_{zz} \nu - E\alpha\Delta T) + E\Delta\epsilon_{xx}}{(1 - \nu^2)} \\ \Delta\sigma_{yy} &= \frac{\nu(1 + \nu)(\Delta\sigma_{zz} \nu - E\alpha\Delta T) + E\Delta\epsilon_{xx}}{(1 - \nu^2)} \end{aligned} \quad (22)$$

For elastic-plastic relaxation, the increments of stress for σ_{xx} and σ_{yy} are calculated as

$$\begin{aligned} \Delta\sigma_{yy} &= \frac{\left(-\frac{\nu}{E} + \frac{1}{h} n_{xx} n_{yy}\right)(C - \alpha\Delta T) - \left(\frac{\nu}{E} + \frac{1}{h} n_{xx} n_{xx}\right)(D - \alpha\Delta T)}{\left[\left(-\frac{\nu}{E} + \frac{1}{h} n_{xx} n_{yy}\right)^2 - \left(\frac{\nu}{E} + \frac{1}{h} n_{xx} n_{xx}\right)\left(\frac{\nu}{E} + \frac{1}{h} n_{yy} n_{yy}\right)\right]} \\ \Delta\sigma_{xx} &= \frac{D - \left(\frac{\nu}{E} + \frac{1}{h} n_{xx} n_{xx}\right)\Delta\sigma_{yy} - \alpha\Delta T}{-\frac{\nu}{E} + \frac{1}{h} n_{xx} n_{yy}} \end{aligned} \quad (23)$$

where

$$\begin{aligned} C &= \Delta\epsilon_{xx} + \left(\frac{\nu}{E} - \frac{1}{h} n_{zz} n_{zz}\right) \dot{\sigma}_{zz}^* - \frac{2}{h} \Delta\tau_{xz}^* n_{xz} n_{xx} \\ D &= \left(\frac{\nu}{E} - \frac{1}{h} n_{zz} n_{zz}\right) \dot{\sigma}_{zz}^* - \frac{2}{h} \Delta\tau_{xz}^* n_{xz} n_{yy} \end{aligned} \quad (24)$$

The remaining stress on the ground surface is called micro-grinding-induced residual stress, which is calculated after the

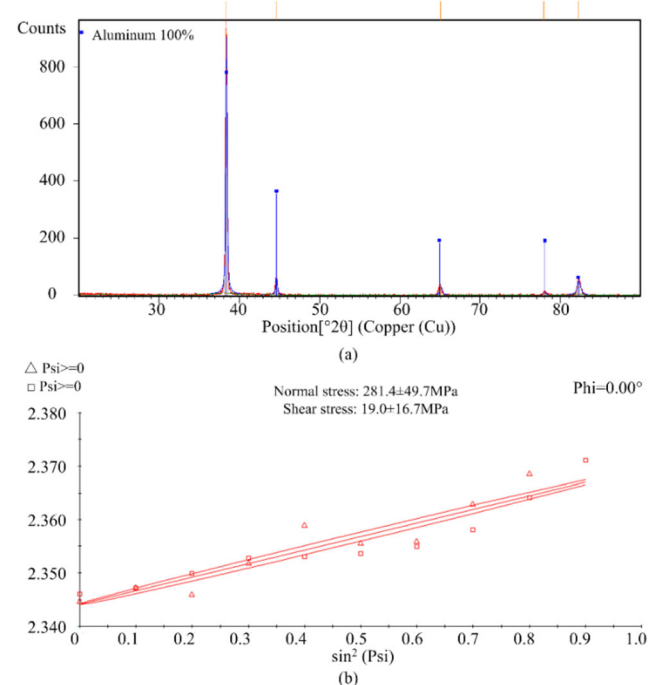


Fig. 7 a XRD patterns and b the $2\theta - \sin^2\psi$ diagram of the 7075 samples

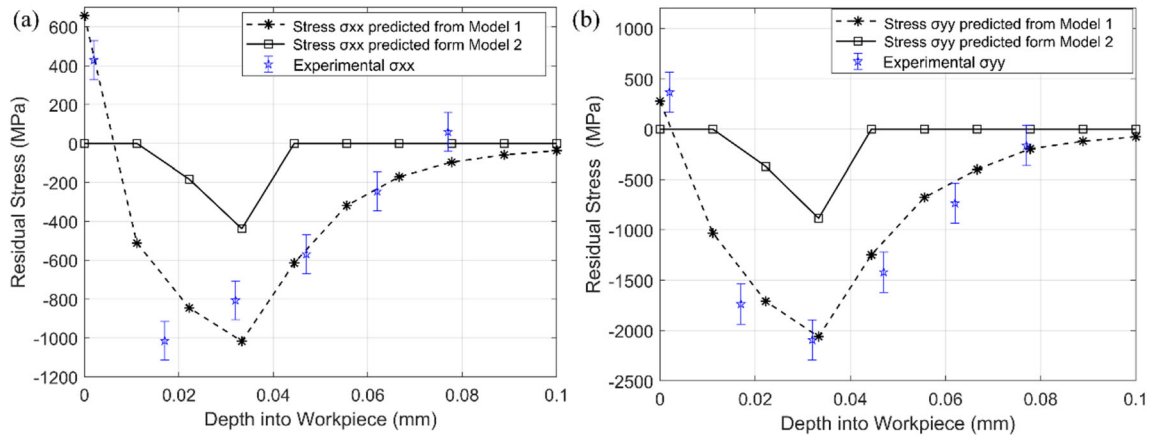


Fig. 8 The comparison result of case no. 1 in (a) x direction and (b) y direction

loading and relaxation process. The calculation procedure chart of residual stress is shown in Fig. 5.

3 Experiments and measurements

Micro-grinding experiments were performed on a miniaturized CNC grinding tool as shown in Fig. 6a. The structure and the performance refer to Ref. [31].

The thermocouple method is utilized to measure the micro-grinding temperature in this investigation. A contacting single-pole thermocouple of nickel chromium and nickel silicon, as shown in Fig. 6b, are used to measure the surface temperatures in the micro-grinding zone with the USB-TC01 capturing the data. The thermocouple are buried in the grooves on the workpiece, as shown in Fig. 6c. CBN grinding wheel 85412-BM was used with a diameter of 3 mm and 240~270 grits, the topography of which is shown in Fig. 6d. The wheel topography was experimentally analyzed. The topography parameters (fitting parameters A_s and K_s , edge radius r , and cone angle ψ) of abrasive grit are obtained (Table 2).

Due to the time and cost constraints of residual stress measurement, only 3 groups of experiments were conducted to

measure the residual stress for model validation, and each group was repeated 3 times. In addition, sample 4 with the Taylor factor of 9.75 only was chosen for the experiments. The micro-grinding parameter combinations are shown in Table 3.

In this paper, the residual stresses were measured on the PANalytical Empyrean X-ray diffraction machine. The Empyrean is a basic theta-two-theta diffractometer with a reflection-transmission spinner in place, which has an incident beam mirror and a fast linear detector (Pixel Medipix 3D). The work current and voltage of the X-ray tube source are 40 mA and 45 kV with Cu anode, respectively.

For sample preparation, Struers electropolisher LectroPol-5 was used to remove layers from the specimen. By adjusting the input voltage to 50 V, the flow rate to 15 mm³/s, and the polishing time to 60 s, a polishing depth of 15 μm was obtained. The polishing depth was measured by the Dektak profilometer. The residual stress was measured at a 15-μm interval up to 0.1 mm depth into the workpiece.

The recorded normal stress in tangential direction on the surface of specimen is presented for demonstration. Figure 7 shows the XRD patterns and the $2\theta - \sin^2\psi$ diagram of the 7075 samples.

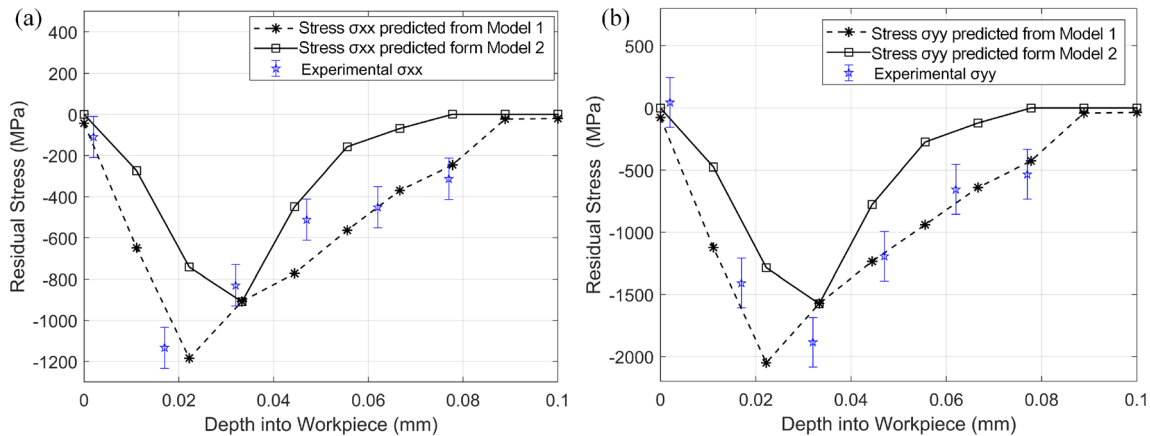


Fig. 9 The comparison result of case no. 2 in (a) x direction and (b) y direction

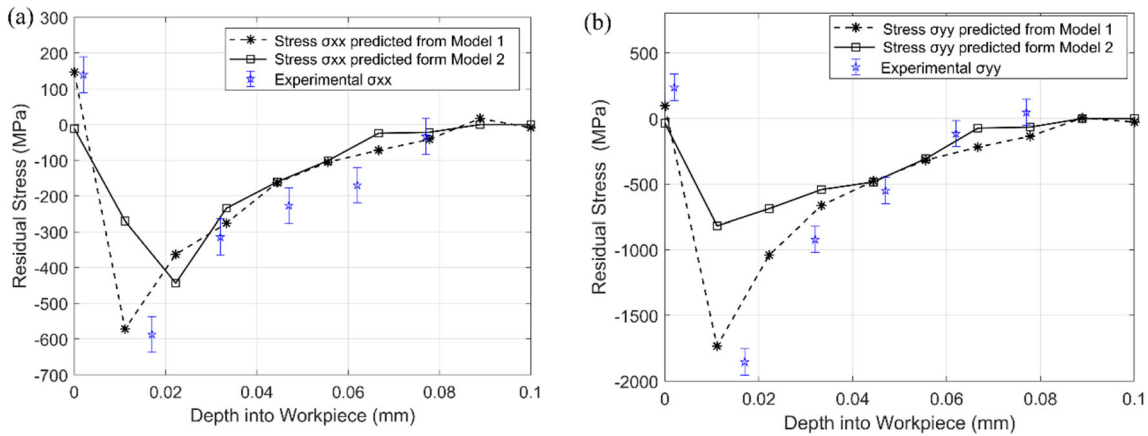


Fig. 10 The comparison result of case no. 3 in (a) x direction and (b) y direction

As shown in Fig. 7a, the peaks occur at 2θ of 38.3852, 44.6012, 65.0696, 77.9190, and 82.2070 with the corresponding height of 936.60, 72.03, 29.60, 10.01, and 51.10 counts. The pattern is analyzed using the software of HighScorePlus, and the single phase is aluminum with the PDF code of 01-089-2837 and displacement [2θ] of 0.004. Figure 7b shows the $2\theta - \sin^2\psi$ diagram obtained from the X-ray measurements made at nine ψ angles. The slope of the $2\theta - \sin^2\psi$ plot is computed by the least square method [36], and the normal stress is then obtained.

4 Model validation

The analytical model of residual stress is validated by experimental data. The stress loading histories are calculated by Eq. (6) and Eq. (8). After the machining tool passes, the released stresses are calculated by Eq. (15) and (16). In addition, the proposed Model 1, which considers the variation of Taylor factor in the flow stress and the plastic modulus, is also compared to Model 2, which takes Taylor factor as a fix value of 3.06 [37]. The predictions and measured data of residual stress

are compared as shown in Figs. 8, 9, and 10, in which, the predicted data of residual stress are successive and the value of any depth into workpiece could be calculated. The measured data is compared to the predicted value plotted on the data dash line on the same depth into workpiece.

From the comparison, it is observed that Model 1 is able to match the measured data with a 10.3% average error in tangential direction and a 19.7% average error in normal direction, while Model 2 cannot match the measured data with a 47.4% average error in tangential direction and a 45.2% average error in normal direction.

In Fig. 8, it is seen that the tendencies of σ_{xx} and σ_{yy} are nearly the same which is due to the distribution of mechanical stresses induced by micro-plastic deformation that are similar in tangential and traverse directions. In addition, the difference between the modeling and experimental residual stresses is large at shallow depth for case no. 1. The possible reasons are summarized as follows: (1) the surface oxidation in the residual stress measurement; (2) the microstructure evolution-induced residual stress which is not considered in the predictive model. Furthermore, compressive residual stresses on the machined surface are usually beneficial since they increase

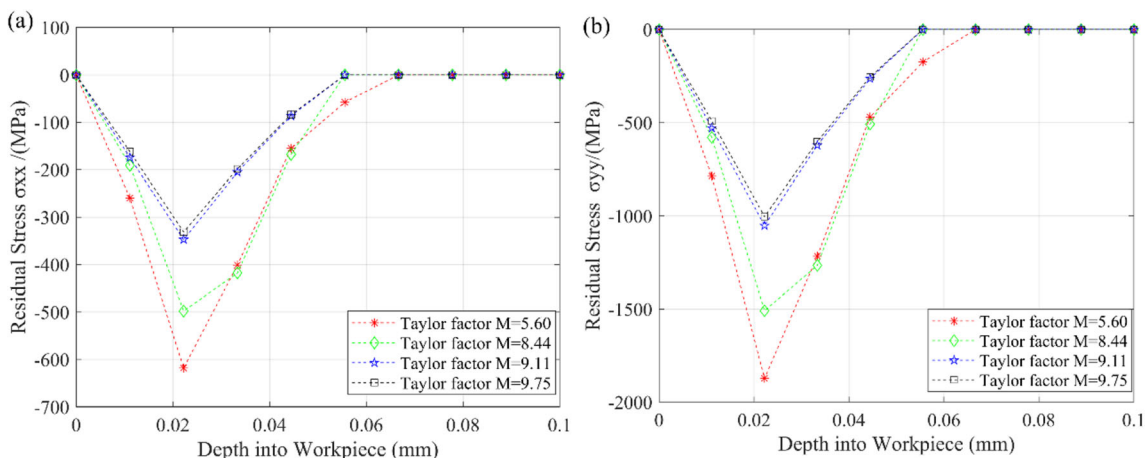


Fig. 11 Residual stresses of different Taylor factor in (a) x direction and (b) y direction

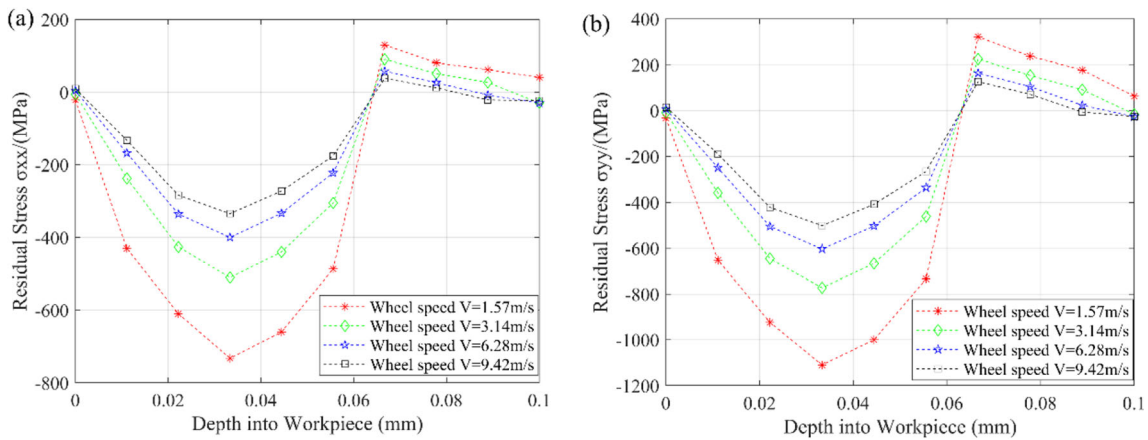


Fig. 12 Residual stresses of different wheel speed in (a) x direction and (b) y direction

both fatigue strength and resistance to corrosion cracking imposed by stress.

The above comparisons indicate that predictions from the proposed residual stress model considering the variation of Taylor factor show a better agreement with the measurements. Improved accuracy suggests that the proposed models of Taylor factor, flow stress, and plastic modulus are effective and reliable.

5 Effects of Taylor factor and grinding parameters on residual stress

To better understand the effects of grinding parameters on residual stress induced by micro-grinding, the sensitivity analysis is conducted and presented in this section.

In addition, Taylor factor, as the parameter to quantify the COs and the corresponding ODF of workpiece material, is also chosen in sensitivity analysis of residual stress. Through analyzing the sensitivity of residual stress to Taylor factor, the effect of Taylor factor to the residual stress could be displayed directly. As a result, it will be an effective method to direct the material preprocessing.

Figure 11 shows the comparison between the residual stresses under different Taylor factor and same grinding condition of 6.28 m/s wheel speed, 10 μm depth of cut, and 10 mm/min feed rate. It is observed that compressive stress occurs on the machined surface when the Taylor factor is in the range from 5.60 to 9.75 on both tangential and traverse directions; maximum compressive stress decreases with increasing Taylor factor; and the penetration of the residual stress profile decreases with increasing Taylor factor as well. The results agree excellently with the earlier result reported by Pen et al. [38]; the distributions of stress are various with different COs. Higher values of stress were observed in the regions of the dislocation emission with a higher Taylor factor, and the stress layer was thinner under the $\begin{bmatrix} 1 & 1 & 1 \end{bmatrix}$ orientation setup with a lower Taylor factor than others. In addition, Liang et al. [39] reported that compressive stress is produced on the surface of nanometric cutting of the plastic material, and the stress increases then decreases with the cutting depth, which is in excellent agreement with the prediction.

Figure 12 shows the comparison of residual stress under different wheel speed and same grinding condition of 10 mm/min feed rate, 10 μm depth of cut, and 5.60 Taylor factor. The results show that tensile stress occurs on the machined surface

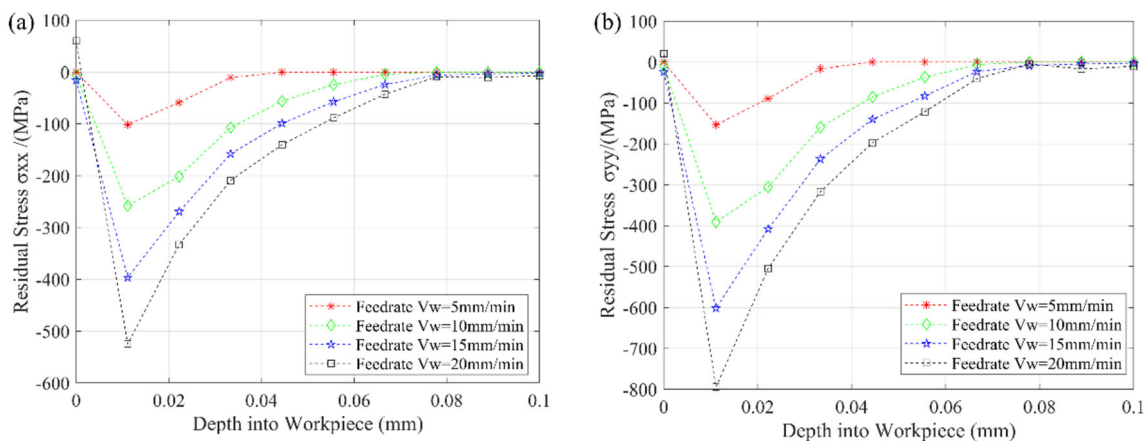


Fig. 13 Residual stresses of different feed rate in (a) x direction and (b) y direction

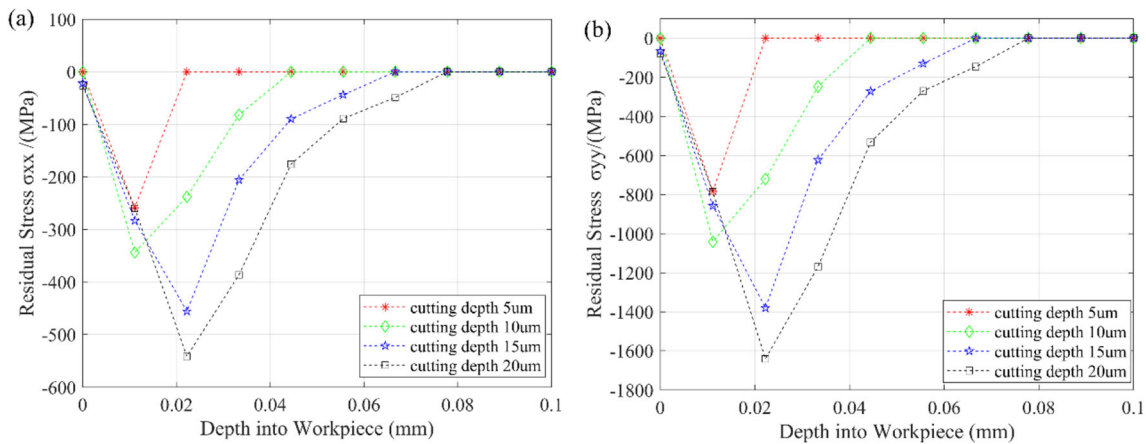


Fig. 14 Residual stresses of different depth of cut in (a) x direction and (b) y direction

when wheel speed is larger than a critical value; maximum compressive stress decreases with increasing wheel speed on both tangential and traverse directions; tensile stress occurs in the subsurface and the maximum tensile stress decreases with increasing wheel speed; and the penetration of the residual stress decreases with increasing wheel speed as well.

Figure 13 shows the comparison of residual stress under different feed rates and same grinding condition of 6.28 m/s wheel speed, 10 μm depth of cut, and 5.60 Taylor factor. It is observed that compressive stress occurs on the machined surface when the feed rate is smaller than a critical value on both tangential and traverse directions; maximum compressive stress increases with an increasing feed rate on both tangential and traverse directions. Moreover, the penetration of the residual stress slightly increases with the increase of feed rate.

Figure 14 shows the comparison of residual stress under different depth of cut and same feed rate of 10 mm/min, speed wheel of 6.28 m/s, and Taylor factor of 5.60. It is concluded that compressive stress occurs on the machined surface in the range from 5 to 20 μm on both tangential and traverse directions; maximum compressive stress increases with increasing cutting depth on both tangential and traverse directions. Moreover, the penetration of the residual stress increases significantly with the increase of depth of cut.

6 Conclusion

In this research, an analytical model is developed for the prediction of micro-grinding-induced residual stress incorporating the mechanical and thermal loading. Additionally, the Taylor factor model is proposed to quantify the effect of material CO on flow stress and plastic modulus model.

The predicted residual stresses from the proposed model are compared to the measurement data. The results show that the predictions from the model considering the variation of Taylor factor agree better with the measurements with a 37.1% average

error in the tangential direction, and a 25.5% average error in the normal direction. The discrepancy of the maximum tensile stress, the compression stress, and the penetration of residual stress, between the prediction and experimental result, is acceptable. It can be drawn that the Taylor factor model is capable of predicting the effect of CO on the residual stress.

The sensitivity of the residual stress to the process parameters is analyzed. The analysis shows that, with an increasing Taylor factor, the maximum compressive stress decreases on both tangential and traverse directions, and the penetration of the residual stress slightly decreases; with an increasing wheel speed, the maximum tensile and compressive stresses decrease on both tangential and traverse directions, and the penetration of the residual stress slightly decreases; with an increasing feed rate, the maximum compressive stress increases on both tangential and traverse directions, and the penetration of the residual stress profile slightly increases; with an increasing depth of cut, the maximum compressive stress increases on both tangential and traverse directions, and the penetration of the residual stress profile increases. It is illustrated that a more compressive residual stress can be induced by micro-grinding under lower grinding wheel speed, smaller Taylor factor, higher feed rate, and larger depth of cut, within the exploded range.

Even though many factors are analyzed by experiment and modeling, the critical factors to the final residual stress were not analyzed in the paper. In the further analysis, it is necessary to analyze the critical factor by response surface methodology (RSM) or analysis of variance (ANOVA).

Acknowledgements The project was supported by Shanghai Pujiang Program (20PJ1404700).

References

1. Pratap A, Patra K, Dyakonov AA (2016) Manufacturing miniature products by micro-grinding: a review. *Proc Eng* 150:969–974. <https://doi.org/10.1016/j.proeng.2016.07.072>

2. Wu Q, Li DP (2014) Analysis and X-ray measurements of cutting residual stresses in 7075 aluminum alloy in high speed machining. *Int J Precis Eng Manuf* 15(8):1499–1506. <https://doi.org/10.1007/s12541-014-0497-4>
3. Nie Z, Wang G, Wang L, Rong Y (2019) A coupled thermomechanical modeling method for predicting grinding residual stress based on randomly distributed abrasive grains. *J Manuf Sci Eng* 141(8). <https://doi.org/10.1115/1.4043799>
4. Kruszyński BW, Wójcik R (2001) Residual stress in grinding. *J Mater Process Technol* 109(3):254–257. [https://doi.org/10.1016/S0924-0136\(00\)00807-4](https://doi.org/10.1016/S0924-0136(00)00807-4)
5. Mahdi M, Zhang L (1999) Applied mechanics in grinding. Part 7: Residual stresses induced by the full coupling of mechanical deformation, thermal deformation and phase transformation. *Int J Mach Tools Manuf* 39(8):1285–1298. [https://doi.org/10.1016/S0890-6955\(98\)00094-7](https://doi.org/10.1016/S0890-6955(98)00094-7)
6. Mahdi M, Zhang L (1998) Applied mechanics in grinding - vi. Residual stresses and surface hardening by coupled thermo-plasticity and phase transformation. *Int J Mach Tools Manuf* 38(10-11):1289–1304. [https://doi.org/10.1016/S0890-6955\(97\)00134-X](https://doi.org/10.1016/S0890-6955(97)00134-X)
7. Mahdi M, Zhang L (1997) Applied mechanics in grinding - v. Thermal residual stresses. *Int J Mach Tools Manuf* 37(5):619–633. [https://doi.org/10.1016/S0890-6955\(96\)00055-7](https://doi.org/10.1016/S0890-6955(96)00055-7)
8. Malkin S (2008) Grinding technology theory and applications of machining with abrasives. Industrial Press, New York
9. Fergani O, Shao Y, Lazoglu I, Liang SY (2014) Temperature effects on grinding residual stress. *Procedia CIRP* 14:2–6. <https://doi.org/10.1016/j.procir.2014.03.100>
10. Shao Y, Fergani O, Li B, Liang SY (2016) Residual stress modeling in minimum quantity lubrication grinding. *Int J Adv Manuf Technol* 83(5):743–751. <https://doi.org/10.1007/s00170-015-7527-y>
11. Shi XL, Xiu SC, Su HL (2019) Residual stress model of pre-stressed dry grinding considering coupling of thermal, stress, and phase transformation. *Adv Manuf* 7(4):401–410. <https://doi.org/10.1007/s40436-019-00280-3>
12. Shen S, Li B, Guo W (2019) Experimental study on grinding-induced residual stress in c-250 maraging steel. *Int J Adv Manuf Technol* 106:953–967. <https://doi.org/10.1007/s00170-019-04655-5>
13. Guo J, Fu H, Pan B, Kang R (2019) Recent progress of residual stress measurement methods: a review. *Chin J Aeronaut*. <https://doi.org/10.1016/j.cja.2019.10.010>
14. Zhu D, Feng X, Xu X, Yang Z, Li W, Yan S, Ding H (2020) Robotic grinding of complex components: a step towards efficient and intelligent machining – challenges, solutions, and applications. *Robot Comput Integr Manuf* 65:101908. <https://doi.org/10.1016/j.rcim.2019.101908>
15. Zhao M, Ji X, Liang SY (2018) Influence of aa7075 crystallographic orientation on micro-grinding force. *Proc Inst Mech Eng B J Eng Manuf* 233(8):1831–1843. <https://doi.org/10.1177/0954405418803706>
16. Zhao M, Ji X, Li B, Liang SY (2016) Investigation on the influence of material crystallographic orientation on grinding force in the micro-grinding of single-crystal copper with single grit. *Int J Adv Manuf Technol* 90(9-12):3347–3355. <https://doi.org/10.1007/s00170-016-9605-1>
17. Park HW, Liang SY (2008) Force modeling of micro-grinding incorporating crystallographic effects. *Int J Mach Tools Manuf* 48(15):1658–1667. <https://doi.org/10.1016/j.ijmactools.2008.07.004>
18. Shen S, Li B, Guo W (2019) Residual stresses distributions in grinding of 3J33 maraging steel with miniature electroplated CBN wheel, The 5th International Conference on Mechatronics and Mechanical Engineering 256
19. Wu C, Pang J, Li B, Liang SY (2019) High-speed grinding of hip-sic ceramics on transformation of microscopic features. *Int J Adv Manuf Technol* 102(5-8):1913–1921. <https://doi.org/10.1007/s00170-018-03226-4>
20. Jiang X, Kong X, Zhang Z, Wu Z, Ding Z, Guo M (2020) Modeling the effects of undeformed chip volume (UCV) on residual stresses during the milling of curved thin-walled parts. *Int J Mech Sci* 167. <https://doi.org/10.1016/j.ijmecsci.2019.105162>
21. Ding ZS, Sun GX, Guo MX, Jiang XH, Li BZ, Liang SY (2020) Effect of phase transition on micro-grinding-induced residual stress. *J Mater Process Technol* 281:281. <https://doi.org/10.1016/j.jmatprotec.2020.116647>
22. Feng YX, Hsu FC, Lu YT, Lin YF, Lin CT, Lin CF, Lu YC, Liang SY (2019) Residual stress prediction in ultrasonic vibration-assisted milling. *Int J Adv Manuf Technol* 104(5-8):2579–2592. <https://doi.org/10.1007/s00170-019-04109-y>
23. Feng YX, Hung TP, Lu YT, Lin YF, Hsu FC, Lin CF, Lu YC, Liang SY (2019) Residual stress prediction in laser-assisted milling considering recrystallization effects. *Int J Adv Manuf Technol* 102(1-4):393–402. <https://doi.org/10.1007/s00170-018-3207-z>
24. Feng YX, Hung TP, Lu YT, Lin YF, Hsu FC, Lin CF, Lu YC, Liang SY (2020) Inverse analysis of the residual stress in laser-assisted milling. *Int J Adv Manuf Technol* 106(5-6):2463–2475. <https://doi.org/10.1007/s00170-019-04794-9>
25. Pan ZP, Shih DS, Garmestani H, Liang SY (2019) Residual stress prediction for turning of ti-6al-4v considering the microstructure evolution. *Proc Inst Mech Eng B-J Eng Manuf* 233(1):109–117. <https://doi.org/10.1177/0954405417712551>
26. Li L, Shen LM, Proust G (2014) A texture-based representative volume element crystal plasticity model for predicting Bauschinger effect during cyclic loading. *Mater Sci Eng A Struct* 608:174–183. <https://doi.org/10.1016/j.msea.2014.04.067>
27. Wang JS, Hsieh CC, Lin CM, Chen EC, Kuo CW, Wu WT (2014) The effect of residual stress relaxation by the vibratory stress relief technique on the textures of grains in aa 6061 aluminum alloy. *Mater Sci Eng A Struct* 605:98–107. <https://doi.org/10.1016/j.msea.2014.03.037>
28. Li C, Li X, Wu Y, Zhang F, Huang H (2019) Deformation mechanism and force modelling of the grinding of YAG single crystals. *Int J Mach Tools Manuf* 143:23–37. <https://doi.org/10.1016/j.ijmactools.2019.05.003>
29. Wang L, Yu H, Lee Y-S, Kim M-S, Kim H-W (2016) Effect of microstructure on hot tensile deformation behavior of 7075 alloy sheet fabricated by twin roll casting. *Mater Sci Eng A* 652:221–230. <https://doi.org/10.1016/j.msea.2015.11.079>
30. Jaeger JC (1942) Moving sources of heat and temperature at sliding contacts. *J Proc R Soc NSW* 76(3):203
31. Zhao M, Ji X, Liang SY (2019) Force prediction in micro-grinding maraging steel 3j33b considering the crystallographic orientation and phase transformation. *Int J Adv Manuf Technol* 103(5-8):2821–2836. <https://doi.org/10.1007/s00170-019-03724-z>
32. Zhao M, Ji X, Liang SY (2019) Micro-grinding temperature prediction considering the effects of crystallographic orientation and the strain induced by phase transformation. *Int J Precis Eng Manuf* 20(11):1861–1876. <https://doi.org/10.1007/s12541-019-00180-3>
33. Timoshenko S, Goodier J (1970) Theory of elasticity. McGraw-Hill, New York.
34. Saif MTA, Hui CY, Zehnder AT (1993) Interface shear stresses induced by non-uniform heating of a film on a substrate. *Thin Solid Films* 224:159–167
35. McDowell DL (1997) Approximate algorithm for elastic-plastic two-dimensional rolling/sliding contact. *Wear* 211(2):237–246
36. Lee D-W, Cho S-S (2011) Comparison of x-ray residual stress measurements for rolled steels. *Int J Precis Eng Manuf* 12(6):1001–1008. <https://doi.org/10.1007/s12541-011-0133-5>

37. Justinger H, Hirt G (2009) Estimation of grain size and grain orientation influence in microforming processes by Taylor factor considerations. *J Mater Process Technol* 209(4):2111–2121. <https://doi.org/10.1016/j.jmatprotec.2008.05.008>
38. Pen HM, Liang YC, Luo XC, Bai QS, Goel S, Ritchie JM (2011) Multiscale simulation of nanometric cutting of single crystal copper and its experimental validation. *Comput Mater Sci* 50(12):3431–3441. <https://doi.org/10.1016/j.commatsci.2011.07.005>
39. Liang YC, Pen HM, Bai QS (2009) Molecular dynamics simulation of nanometric cutting characteristics of single crystal cu. *Acta Metall Sin* 45:1205–1210

Publisher's note Springer Nature remains neutral with regard to jurisdictional claims in published maps and institutional affiliations.